Electronic Journal of Mathematical Analysis and Applications
Vol. 13(2) July 2025, No.11.
ISSN: 2090-729X (online)
ISSN: 3009-6731(print)
http://ejmaa.journals.ekb.eg/

TRANSIENT MOVEMENT OF A HYDROPHOBIC PARTICLE IN A CAVITY CONTAINING A BRINKMANN MEDIUM

M.S. FALTAS, E.I. SAAD, H.H. SHERIEF, A.S.AAMER

Abstract. This study investigates the transient motion of a hydrophobic colloidal spherical particle within a concentric cavity filled with a polymer gel, under low Reynolds number conditions. The polymer gel is modeled as a porous medium with a specified permeability, determined through experimental measurements. Fluid movement within the porous matrix is induced by a sudden application of a steady body force along the line connecting the particle and cavity centers. The transient Brinkman equation governs the fluid dynamics within the cavity and is analytically solved using the Laplace transform method. The study highlights the long-range hydrodynamic interactions between the colloidal particle and the surrounding polymer gel medium, leading to an analytical expression for the transient velocity of the particle as a function of key system parameters. This work provides insight into particle mobility in polymer gels, with implications for applications in controlled drug delivery and biocompatible material design.

1. Introduction

When an external force field is suddenly imposed on a suspension of colloidal particles, the particles initiate motion characterized by a time-dependent transient velocity. This velocity eventually stabilizes as time progresses towards infinity. The movements of minute particles within a porous medium, particularly at extremely low Reynolds numbers, remain a subject of widespread interest among researchers across diverse fields including chemical, biomedical, mechanical, civil, and environmental engineering. While many of these movements are fundamental in nature, they contribute significantly to our comprehension of various practical systems such as sedimentation, agglomeration, electrophoresis, microfluidics, cellular motion within blood vessels [14, 17], suspension rheology, spray drying, and aerosol technology.

2020 *Mathematics Subject Classification.* 34A12, 76D07, 76S05.
Key words and phrases. Transient velocity, slow motion, polymer gel, concentric cavity.
Submitted April 29, 2025. Revised May 19, Accepted July 9, 2025.

The complexity of the gel material arises from both the long-range hydrodynamic interaction and the steric effect resulting from friction between the gel skeleton and migrating particles: The short-range steric interaction arising from the friction between the particle and the gel. The significance of the short-range effect becomes pronounced when the ratio between the pore size of a gel polymer and the particle size is small. Conversely, if the ratio is large, the long-range hydrodynamic effect takes precedence. In dilute gel situations, where the particle's dimensions are significantly smaller than those of the gel pores, the long-range hydrodynamic interaction prevails. In this study, we focus on a dilute gel medium and analyze the long-range hydrodynamic interaction between the particle and the polymer gel medium using the Brinkman–Debye–Bueche model [8, 12]. Brady [5] introduced a theory to explain hindered diffusion through fibrous media, where the diffusivity ratio is determined by the multiplication of a hydrodynamic factor and a steric factor. This model has been validated by various researchers, including Johansson and Lofroth [24], Allison et al.[3], and others. Studies conducted by Allison et al. [3], Tsai et al. [46], and Hsu et al. [23] have demonstrated that the short-range steric effect in particle-polymer interactions can be accurately described by Brady's model [5].

Extensive research has been conducted on the movement of Newtonian fluid through porous materials, which holds significant practical implications. The Brinkman equation [8] often characterizes the viscous flow within such porous mediums, effectively accounting for the interplay between pressure gradients and viscosity-induced drag forces, alongside the damping effects originating from the porous structure. Considerable focus has been dedicated over time to examining the dynamics of particles traversing porous media, as evidenced by studies[26, 35, 11, 43, 21, 6, 10, 16, 31, 19, 18].

While the fundamental equations governing the slow movements of particles within viscous or porous mediums were primarily developed for steady-state conditions, understanding their transient dynamics is equally significant [32, 22, 20, 29, 30]. The comprehension of the temporal changes in particle velocity is relevant to the practical applications of diverse movements in colloidal dynamics, spanning from milliseconds to seconds in scale. [13, 47, 41, 40, 39, 38, 27, 36, 30, 28, 42, 4]. Conversely, investigations have been conducted on the transient responses of particle velocity following a sudden alteration in external force, considering both no-slip and slip cases for solid particles or droplets [34, 25].

In this article, a semi-analytical approach is employed to examine the time-dependent translational motion of a hydrophobic colloidal spherical particle in a concentric position within a spherical cavity filled with polymer gel material, experiencing a sudden application of a uniform body force field along the diameter connecting their centers. Slip behavior is permitted for the fluid at both the particle and cavity surfaces. The primary goal of this research is to broaden and generalize the discoveries made by Yu and Keh [9] to include the porous medium case, with particular attention was given to the impact of the Darcy-Brinkman model during transient flow. To achieve this, Laplace transform techniques are utilized to solve the time-dependent Brinkman equations governing fluid velocity. In addition, the study derives the rectilinear acceleration of the particle.

A practical physical application of the present model could be in the design and optimization of drug delivery systems, especially those involving hydrophobic colloidal particles encapsulated in a polymer gel matrix. In drug delivery, controlled release of therapeutic agents is often desired, and this model helps simulate how a drug-loaded colloidal particle would move within a polymer gel after being subjected to external forces, which might represent body forces induced by external magnetic, electric, or acoustic fields [15]. Since the gel in this model behaves as a porous medium with specific permeability, it mimics a realistic physiological environment where drugs are embedded in hydrogels or other porous materials. Such simulations are valuable for designing drug carriers because they allow researchers to predict how rapidly a particle will reach target tissue, how long it remains in certain regions, and how it interacts with the surrounding medium. The analytical expression for transient velocity could aid in tuning parameters like particle size, surface hydrophobicity, and gel permeability to optimize release profiles and targeting efficiency [45, 33].

2. Unsteady Brinkman equation with initial and boundary conditions

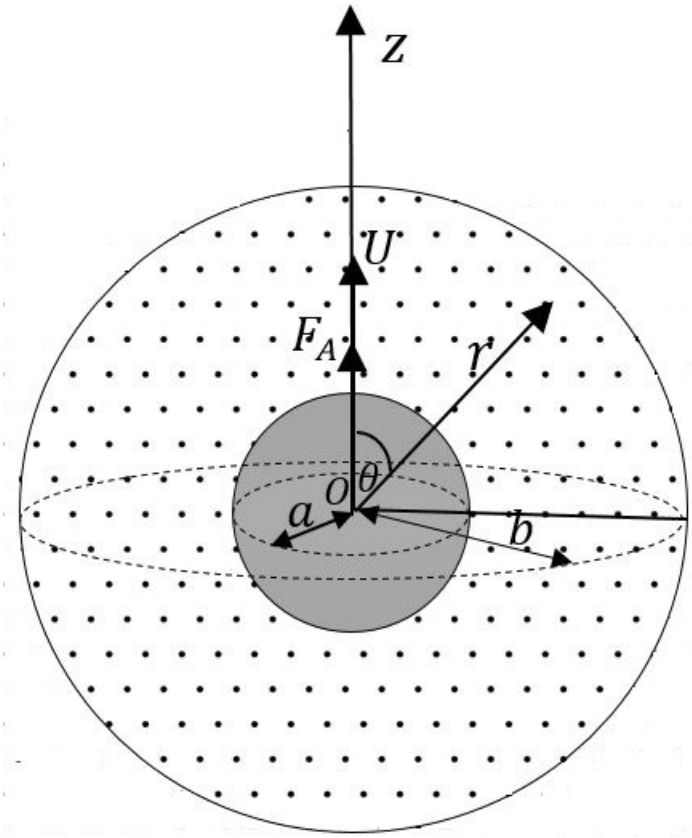

Figure 1. Geometrical sketch for a slip-Brinkman flow between hydrophobic spherical particle and cavity

We examine the transient movement of a spherical colloidal particle with a radius of a as it migrates concentrically within a spherical cavity of radius b, which is filled with porous material. This porous medium is saturated with an incompressible Newtonian fluid, and its motion is induced by a sudden application of a body force, as depicted in Fig.1. At the onset time, $t = 0$, a constant force $F_A\vec{e}_z$, where $\vec{e}_z$ represents the unit vector in the z direction, is applied to the initially stationary particle and persists thereafter. Here, the force F_A could be the difference between the gravitational force and the buoyant force. We consider that both the surface of the particle and the inner surface of the cavity are hydrophobic, hence we can assume slip at their surfaces. In this study, we may regard the porous medium as a polymer gel, under the assumption that long-range hydrodynamic effects occur. This necessitates that the ratio between the pores of the gel and the particle size is large, indicating that the gel medium is dilute.

Under low Reynolds number conditions $N_R(N_R << 1)$, the velocity distribution $\vec{u}$ and hydrodynamic pressure profile p of the fluid are governed by the transient Brinkman equation:

$$\frac{\rho}{\varphi}\frac{\partial \vec{u}}{\partial t} = \widetilde{\mu}\nabla^2\vec{u} - \frac{\mu}{K}\vec{u} - \nabla p, \tag{1}$$

along with the conservation of mass,

$$\nabla \cdot \vec{u} = 0. \tag{2}$$

Here ρ is the density of the fluid, K is the permeability of the porous materiel, $\widetilde{\mu}$ is the effective viscosity and φ is the porosity. In general, $\widetilde{\mu}$ is different from μ. Brinkman equation (1) reduces to Darcy's equation when $\widetilde{\mu} \to 0$ and to the Stokes equation when $K \to \infty$. Breugem [7] suggested that the effective viscosity $\widetilde{\mu}$ is a function of the geometrical structure and the porosity of the porous medium. However, many authors e.g. [10, 37] considered $\widetilde{\mu} = \mu$. The spherical coordinate system (r, θ, ϕ) places the center of the particle at the origin, with $\theta = 0$ representing the axis in the z direction with corresponding unit vectors $(\vec{e}_r, \vec{e}_\theta, \vec{e}_\phi)$. The flow within the spherical cavity exhibits axial symmetry and is independent of ϕ.

The symmetrical nature of the flows allows us to establish stream function, denoted as ψ, which is linked to velocity through the equation:

$$\vec{u}(r,\theta) = u_r\vec{e}_r + u_\theta\vec{e}_\theta = -\nabla \wedge \left(\frac{\psi}{r\sin\theta}\vec{e}_\phi\right). \tag{3}$$

It is important to observe that equation (3) is in accordance with the conservation of mass stated in equation (2). By applying the curl operation to equation (1) and utilizing equation (3), we derive the differential equation governing the stream function ψ as

$$E^2\left(E^2 - \lambda^2 - \frac{1}{\nu}\frac{\partial}{\partial t}\right)\psi = 0, \tag{4}$$

with pore-average pressure gradient as

$$\nabla p = -\frac{\widetilde{\mu}}{r\sin\theta}\left(\frac{\vec{e}_r}{r}\frac{\partial}{\partial\theta} - \vec{e}_\theta\frac{\partial}{\partial r}\right)\left(E^2 - \lambda^2 - \frac{1}{\nu}\frac{\partial}{\partial t}\right)\psi, \tag{5}$$

where $E^2 \equiv \frac{\partial^2}{\partial r^2} + \frac{\sin\theta}{r^2}\frac{\partial}{\partial\theta}\left(\frac{1}{\sin\theta}\frac{\partial}{\partial\theta}\right)$ is the Stokes operator, $\nu = \frac{\varphi\widetilde{\mu}}{\rho}$ is the effective kinematic viscosity, $\lambda = \sqrt{\frac{\mu}{\widetilde{\mu}K}}$ is the permeability parameter characterizing the

porous medium. To address the solution of (4), the initial and boundary conditions must be specified.

The initial and boundary conditions for the volume-averaged velocity vector are

$$t = 0, \quad \vec{u} = 0 \tag{6}$$

$$r = a: \quad u_r = U(t)\cos\theta, \quad u_\theta + U(t)\sin\theta = \beta_1^{-1}\Pi_{r\theta}, \tag{7}$$

$$r = b: \quad u_r = 0, \quad u_\theta = \beta_2^{-1}\Pi_{r\theta}, \tag{8}$$

where $U(t)$ is the transient migration velocity of the spherical particle with $U(0) = 0$ to be determined, β_1, β_2 are, respectively, the sliding friction slip coefficients of the particle and cavity which are depend on the nature of particle and porous medium, and $\Pi_{r\theta}$ is the tangential stress tensor is given by

$$\Pi_{r\theta} = \widetilde{\mu}\left[r\frac{\partial}{\partial r}\frac{u_\theta}{r} + \frac{1}{r}\frac{\partial u_r}{\partial \theta}\right]. \tag{9}$$

We have also the expression of the normal stress as

$$\Pi_{rr} = -p + 2\widetilde{\mu}\frac{\partial u_r}{\partial r}. \tag{10}$$

When β_1 approaches 0, the particle's surface experiences perfect slip, causing the particle to resemble a spherical gas bubble. Conversely, the traditional no-slip boundary condition for the particle and cavity is achieved by allowing β_1 and β_2 to approach infinity.

3. Analysis

The initial and boundary conditions (6)-(9) imply a solution for (4) represented as

$$\psi(r, \theta, t) = g(r, t)\sin^2\theta. \tag{11}$$

The Laplace transform with respect to the time t for a function $g(r, t)$ is defined as

$$\bar{g}(r, s) = \int_0^\infty g(r, t)e^{-st}dt, \tag{12}$$

where the transform is represented by placing a bar over the function and s is the transform parameter. By substituting equation (11) into equation (4) and subsequently applying the Laplace transform, we obtain

$$\left(\frac{d^2}{dr^2} - \frac{2}{r^2}\right)\left(\frac{d^2}{dr^2} - \frac{2}{r^2} - \xi^2\right)\bar{g}(r, s) = 0, \qquad \xi = \sqrt{\lambda^2 + \frac{s}{\nu}}, \tag{13}$$

where we have used the initial condition (6). The boundary conditions (7), (8) are transformed to:

$$\bar{g} = -\tfrac{1}{2}r^2\bar{U}, \quad r = a, \tag{14}$$

$$\frac{d\bar{g}}{dr} + r\bar{U} = b_1\left(r^2\frac{d}{dr}\frac{1}{r^2}\frac{d\bar{g}}{dr} + \frac{2\bar{g}}{r^2}\right), \quad r = a, \tag{15}$$

$$\bar{g} = 0, \quad r = b, \tag{16}$$

$$\frac{d\bar{g}}{dr} = b_2\left(r^2\frac{d}{dr}\frac{1}{r^2}\frac{d\bar{g}}{dr} + \frac{2\bar{g}}{r^2}\right), \quad r = b. \tag{17}$$

Here $b_1 = \widetilde{\mu}/\beta_1$ and $b_2 = \widetilde{\mu}/\beta_2$ are dimensional slip lengths. The general solution of the fourth order differential equation (13) can be written in the following form:

$$\bar{g}(r,s) = \frac{A}{r} + Br^2 + C\left(\frac{1}{r} + \xi\right)e^{-\xi r} + D\left(\frac{1}{r} - \xi\right)e^{\xi r}. \tag{18}$$

The transformed pressure, normal stress and tangential stress are as follows:

$$\bar{p} = p_0 - \widetilde{\mu}\xi^2\left(\frac{A}{r^2} - 2B\right)\cos\theta,\ \bar{\Pi}_{rr} = \widetilde{\mu}\bar{f}_1(r,s)\cos\theta,\ \bar{\Pi}_{r\theta} = \widetilde{\mu}\bar{f}_s(r,s)\sin\theta, \tag{19}$$

where

$$\begin{aligned}\bar{f}_1(r,s) = &\left(\frac{\xi^2}{r^2} + \frac{12}{r^4}\right)A + 2B\xi^2 r + \frac{4C}{r^2}(3 + 3\xi r + \xi^2 r^2)e^{-\xi r}\\ &+ \frac{4D}{r^4}(3 - 3\xi r + \xi^2 r^2)e^{\xi r},\end{aligned} \tag{20}$$

$$\begin{aligned}\bar{f}_2(r,s) = &\frac{6A}{r^4} + \frac{C}{r^4}(\xi^3 r^3 + 3\xi^2 r^2 + 6\xi r + 6)e^{-\xi r}\\ &- \frac{D}{r^4}(\xi^3 r^3 - 3\xi^2 r^2 + 6\xi r - 6)e^{\xi r},\end{aligned} \tag{21}$$

and p_0 is a constant. Inserting (18) into the transformed boundary conditions (14)-(17), we obtain the following set of the four simultaneous equations for determining the unknown constants A, B, C and D ,

$$A + Ba^3 + C(\eta + 1)e^{-\eta} - D(\eta - 1)e^{\eta} = \frac{-1}{2}a^3\bar{U}, \tag{22}$$

$$\left.\begin{aligned}(6\lambda_1 + 1)A - 2Ba^3 + C\big(\lambda_1\eta^3 + (1 + 3\lambda_1)\eta^2 + (1 + 6\lambda_1)(\eta + 1)\big)e^{-\eta}\\ -D\big(\lambda_1\eta^3 - (1 + 3\lambda_1)\eta^2 + (1 + 6\lambda_1)(\eta - 1)\big)e^{-\eta} = a^3\bar{U},\end{aligned}\right\} \tag{23}$$

$$A\sigma^3 + Ba^3 + \sigma^2 C(\sigma + \eta)e^{-\eta/\sigma} + \sigma^2 D(\sigma - \eta)e^{\eta/\sigma} = 0, \tag{24}$$

$$\left.\begin{aligned}&\sigma^3(1 - 6\sigma\lambda_2)A - 2Ba^3\\ &+C\big(\sigma(\sigma^2 + \sigma\eta + \eta^2) - \lambda_2\sigma(6\sigma^3 + 6\sigma^2\eta + 3\sigma\eta^2 + \eta^3)\big)e^{-\eta/\sigma}\\ &+D\big(\sigma(\sigma^2 - \sigma\eta + \eta^2) - \lambda_2\sigma(6\sigma^3 - 6\sigma^2\eta + 3\sigma\eta^2 - \eta^3)\big)e^{-\eta/\sigma} = 0,\end{aligned}\right\} \tag{25}$$

where, $\eta = a\xi = \sqrt{\alpha^2 + a^2 s/\nu}$, $\alpha = a\lambda$, $\lambda_1 = b_1/a$, $\lambda_2 = b_2/a$ and $\sigma = a/b$. Here we document the expression of constant A, as it is the sole constant present in the hydrodynamic drag force exerted on the particle:

$$A = -\frac{a^3\bar{U}(s)}{2\Delta}\big[(c_1 d_3 - d_1 c_3) + 2(c_1 d_2 - d_1 c_2)\big], \tag{26}$$

where

$$\Delta = a_1(c_2 d_3 - d_2 c_3) - c_1(a_2 d_3 - d_2 a_3) + d_1(a_2 c_3 - c_2 a_3), \tag{27}$$

and $a_i, c_i, d_i,\ \ i = 1, 2, 3$ are defined as shown in following expressions,

$$\left.\begin{aligned}
a_1 =&6\lambda_1 + 3,\\
c_1 =&\big(\lambda_1(6 + 6\eta + 3\eta^2 + \eta^3) + (3 + 3\eta + \eta^2)\big)e^{-\eta},\\
d_1 =&\big(\lambda_1(6 - 6\eta + 3\eta^2 - \eta^3) + (3 - 3\eta + \eta^2)\big)e^{\eta},\\
a_2 =&\sigma^3 - 1,\\
c_2 =&(\sigma^3 + \sigma^2\eta)e^{-\eta/\sigma} - (1 + \eta)e^{-\eta},\\
d_2 =&(\sigma^3 - \sigma^2\eta)e^{\eta/\sigma} - (1 - \eta)e^{\eta},\\
a_3 =&2 + \sigma^3 - 6\sigma^4\lambda_2,\\
c_3 =&\big((\sigma^3 + \sigma^2\eta + \sigma\eta^2) - \sigma\lambda_2(6\sigma^3 + 6\sigma^2\eta + 3\sigma\eta^2 + \eta^3)\big)e^{-\eta/\sigma}\\
&+ 2(1 + \eta)e^{-\eta},\\
d_3 =&\big((\sigma^3 - \sigma^2\eta + \sigma\eta^2) - \sigma\lambda_2(6\sigma^3 - 6\sigma^2\eta + 3\sigma\eta^2 - \eta^3)\big)e^{\eta/\sigma}\\
&+ 2(1 - \eta)e^{\eta}.
\end{aligned}\right\} \tag{28}$$

3.1. **The drag force acting on the particle.** Due the axial symmetry of the flow, the drag force acting on the spherical particle is only one force component in the direction of the unit vector $\vec{e}_z$,its transformed version is given by

$$\bar{F_h} = 2\pi\widetilde{\mu}a^2 \int_0^{\pi} \left(\bar{f}_1(a, s)\cos^2\theta - \bar{f}_2(a, s)\sin^2\theta\right)\sin\theta d\theta. \tag{29}$$

Inserting (20) and (21) into (29) and using (22), we obtain

$$\bar{F_h} = \tfrac{4}{3}\pi\widetilde{\mu}\xi^2(3A + a^3\bar{U}). \tag{30}$$

The combined effect of the applied force and hydrodynamic drag acting on the particle is equivalent to the multiplication of its mass and acceleration:

$$F_A + F_h = \tfrac{4}{3}\pi a^3\rho_s\frac{dU}{dt}, \tag{31}$$

where ρ_s is the mass density of the particle. Replacing equation (31) in the Laplace transform of equation (30) gives a formula detailing the particle's migration response to the abruptly applied force:

$$6\pi\widetilde{\mu}a\frac{\bar{U}}{F_A} = \frac{9}{2s}\left(\left(\frac{sa^2}{\nu}\right)\rho^* + 3\eta^2\left(\frac{(c_1d_3 - d_1c_3) + 2(c_1d_2 - d_1c_2)}{2\Delta} - \frac{1}{3}\right)\right)^{-1}, \tag{32}$$

where $\rho^* = \varphi\rho_s/\rho$ is the density ratio between the particle and fluid.

The transient velocity of the particle $U(t)$, can be determined numerically by applying an inverse Laplace transform to the calculated formula (32) of $\bar{U}(s)$, [44, 2, 1].

3.2. **The steady-state particle velocity.** The velocity of the particle, U_∞ as $t \to \infty$ can be calculated as

$$U_\infty = \frac{F_A}{4\pi a\widetilde{\mu}\alpha^2}\left(\frac{(c_1^{'}d_3^{'} - d_1^{'}c_3^{'}) + 2(c_1^{'}d_2^{'} - d_1^{'}c_2^{'})}{2\Delta^{'}} - \frac{1}{3}\right)^{-1}, \tag{33}$$

where,

$$\Delta^{'} = a_1^{'}(c_2^{'}d_3^{'} - d_2^{'}c_3^{'}) - c_1^{'}(a_2^{'}d_3^{'} - d_2^{'}a_3^{'}) + d_1^{'}(a_2^{'}c_3^{'} - c_2^{'}a_3^{'}), \tag{34}$$

and $a_i^{'}, c_i^{'}, d_i^{'},\ i = 1, 2, 3$ are the same as the expressions listed in (28) with η replaced by α.

4. Results and Discussion

The transient velocity $U(t)$ of a particle, momentarily located at the center of a cavity filled with a gel medium, is calculated using the numerical inverse Laplace transform of equation (32). This velocity is then scaled by the steady-state Stokes-law value $F_A/6\pi a\widetilde{\mu}$, and plotted against various values of the scaled elapsed time $\nu t/a^2$, relative density ρ^*, the permeability parameter α of the porous medium, and the non-dimensional slip length of the particle λ_1 and λ_2, respectively, in Figs 2-5. Fig. 6 also exhibit the results of the normalized transient acceleration for the same set of parameters.

Table 1 presents the normalized transient velocity $6\pi\widetilde{\mu}aU/F_A$ of a hydrophobic spherical particle inside a concentric spherical cavity filled with a Brinkman medium under the influence of a suddenly applied body force. The results are given for different configurations of the permeability parameter α, the radius ratio σ, and the scaled time $\nu t/a^2$, assuming no-slip boundary conditions on both the particle and cavity surfaces ($\lambda_1, \lambda_2 = 0$). A significant observation from the table is the behavior of the transient solution under extreme conditions. As the permeability parameter approaches zero ($\alpha \to 0$), the Brinkman medium functions equivalently to a pure Newtonian fluid. As the radius ratio σ approaches zero ($\sigma \to 0$), the cavity expands infinitely, allowing the particle to traverse an unbounded fluid. This situation pertains to the classical transitory motion of a solid particle within a transparent fluid, specifically the scenario examined by Keh [9], in which the particle is an impermeable sphere.

Conversely, when α approaches infinity and σ approaches one ($\alpha \to \infty,\ \sigma \to 1$), the Brinkman medium becomes exceedingly resistant (tending towards Darcy's law), and the cavity tightly confines the particle. This configuration corresponds with the premises of Keh's model for a completely contained solid particle within a Brinkman medium. Notably, the values in the third column of Table 1 ($\alpha = 0$, $\sigma \to 0$) converge precisely with those in the last column, which represent the identical results documented by Keh. This agreement verifies that our transient model accurately replicates Keh's solution as a specific instance in which the particle is an impermeable sphere, hence offering robust validation for both the analytical formulation and the numerical methodology.

Fig. 2 shows the variation of normalized transient velocity $6\pi\widetilde{\mu}aU/F_A$ versus the permeability parameter α for various values of the scaled elapsed time $\nu t/a^2$ under conditions of perfect slip at the particle and cavity surfaces ($\lambda_1, \lambda_2 \to \infty$). The curves correspond to different values of elapsed time and relative density ρ^*, with two representative values of $\rho^* = 0.2$ (solid lines) and $\rho^* = 2$ (dashed lines). The x-axis is labeled with "Stokes flow" on the left, corresponding to low α values (low permeability, or nearly clear fluid), and "Darcian flow" on the right, where α is large, indicating a highly porous medium with limited fluid resistance. For both values of relative density ρ^*, the normalized transient velocity $6\pi\widetilde{\mu}aU/F_A$ decreases with increasing α. Physically, this can be attributed to the effect of permeability on fluid flow resistance. At lower α values (Stokes flow regime), the fluid flows more freely around the particle, leading to higher velocities. As α increases, the porous medium restricts fluid movement, resulting in a reduction in the particle's

TABLE 1. Normalized transient velocity $6\pi\widetilde{\mu}a\frac{U}{F_A}$ at various values of elapsed time $\nu t/a^2$, ρ^* in the case of no-slip surfaces ($\lambda_1 = 0$, $\lambda_2 = 0$). The exact analytic results of Keh. [9] are represented as $\alpha \to \infty$.

		$6\pi\widetilde{\mu}a\frac{U}{F_A}$			
$\nu t/a^2$	ρ^*	$\alpha = 10,\ \sigma \to 1$	$\alpha = 5,\ \sigma = 0.5$	$\alpha = 0,\ \sigma \to 0$	Keh [9]
$\nu t/a^2 = 0.3$					
	0	0	0.0684	0.3712	0.3712
	1	0	0.0684	0.3046	0.3046
	2	0	0.0683	0.2535	0.2535
	3	0	0.0678	0.2155	0.2156
	4	0	0.0668	0.1869	0.1869
	5	0	0.0655	0.1648	0.1648
	6	0	0.0639	0.1472	0.1472
	7	0	0.0622	0.1329	0.1329
	8	0	0.0603	0.1211	0.1211
	9	0	0.0585	0.1112	0.1112
	10	0	0.0566	0.1028	0.1028
	20	0	0.0414	0.0584	0.0584
$\nu t/a^2 = 1$					
	0	0	0.0684	0.5545	0.5546
	1	0	0.0684	0.5163	0.5163
	2	0	0.0684	0.4773	0.4773
	3	0	0.0684	0.4403	0.4404
	4	0	0.0684	0.4067	0.4067
	5	0	0.0684	0.3766	0.3767
	6	0	0.0684	0.3500	0.3501
	7	0	0.0684	0.3265	0.3265
	8	0	0.0684	0.3057	0.3057
	9	0	0.0683	0.2871	0.2872
	10	0	0.0682	0.2706	0.2706
	20	0	0.0653	0.1704	0.1704
$\nu t/a^2 \to \infty$					
Steady state	0	0	0.0684	0.8268	0.8278
	1	0	0.0684	0.8235	0.8245
	2	0	0.0684	0.8200	0.8210
	3	0	0.0684	0.8162	0.8171
	4	0	0.0684	0.8121	0.8130
	5	0	0.0684	0.8078	0.8086
	6	0	0.0684	0.8030	0.8039
	7	0	0.0684	0.7980	0.7988
	8	0	0.0684	0.7926	0.7933
	9	0	0.0684	0.7868	0.7875
	10	0	0.0684	0.7808	0.7814
	20	0	0.0684	0.7087	0.7091

velocity. In the limit as $\alpha \to \infty$ (Darcian flow), the particle's velocity approaches zero because the highly porous medium essentially immobilizes the particle within the gel. Fig. 2 indicates that each curve is labeled with a different value of the scaled elapsed time $\nu t/a^2$, showing how the transient velocity changes over the called elapsed time. For short times (e.g., $\nu t/a^2 = 0.005$), the particle's velocity starts low, as the surrounding fluid has not fully responded to the applied body force. At intermediate times (e.g., $\nu t/a^2 = 0.05,\ 0.5$), as time progresses, the fluid velocity around the particle increases, reaching a peak. At long times, the system approaches a steady state, and the transient velocity stabilizes. The curves labeled $\nu t/a^2 \to \infty$ represent this steady state, showing the final, time-independent normalized velocity.

The solid lines ($\rho^* = 0.2$) and dashed lines ($\rho^* = 2$) represent different particle-to-fluid density ratios. For higher relative density ($\rho^* = 2$), the particle experiences greater inertia, resulting in lower normalized velocities across all times and α values compared to the lower-density particle ($\rho^* = 0.2$). The dependence on ρ^* reflects how inertia impacts the particle's response to the body force; a denser particle moves more slowly due to the added resistance from its mass relative to the surrounding fluid. The figure spans two flow regimes: Stokes flow (low α) and Darcian flow (high α). In the Stokes flow regime, where the permeability parameter is zero, the particle's velocity remains relatively high because the clear fluid allows easy passage. In the Darcian flow regime, where permeability is low (high α), the fluid within the porous medium restricts movement, leading to a gradual decay in velocity toward zero. This plot helps illustrate the impact of permeability, elapsed time, and density on the transient behavior of a colloidal particle within a polymer gel. In applications like drug delivery or biocompatible materials, these parameters can be tuned to control the particle's mobility. For example, higher permeability or a lower relative density can enhance mobility, which might be desirable in cases where rapid diffusion through the medium is needed. Conversely, higher density or lower permeability Fig. 3(a, b, c) show how the normalized transient velocity changes with the non- dimensional slip length λ_1 of the particle, ranging from a "no slip" condition ($\lambda_1 = 0$) to "perfect slip" ($\lambda_1 \to \infty$), for different elapsed times, $\nu t/a^2$ with a fixed slip length of the cavity ($\lambda_2 = 1$). As λ_1 increases, the normalized transient velocity generally tends to increase. This indicates that a larger slip length at the particle surface allows for reduced frictional resistance between the particle and surrounding fluid. Physically, this can enhance particle mobility as the resistance to movement in the fluid decreases with greater slip. Fig. 3(a) indicates that, as α increases, the normalized velocity of the particle decreases across all slip lengths λ_1. For small λ_1 (low-slip conditions), the effect of α is more pronounced, as the particle is subject to high drag from both the fluid viscosity and the porous medium's resistance. For large λ_1 (high-slip conditions), the normalized velocity increases regardless of α, although the overall velocity remains lower for higher α. This suggests that slip at the particle surface can partially mitigate the drag effect imposed by the porous medium. Fig. 3(b) shows the variation of the normalized velocity of the particle for three critical cases of the density ratio: $\rho^* = 0,\ 1$, and ∞. In the case $\rho^* = 0$, the particle has no effective mass, which could represent a case where the particle is neutrally buoyant or experiences no gravitational effects. When $\rho^* = 1$, the particle has the same density as the fluid, introducing inertial effects that may alter its response to the applied force. For $\rho^* \to \infty$, the particle is

very dense, has a large mass, and therefore significant inertia. For $\rho^* = 0$, the particle reaches a higher normalized transient velocity compared to $\rho^* = 1$, as a lighter particle (with effectively zero density) responds more directly to the applied force without inertial resistance. As the time $\nu t/a^2$ increases, the normalized velocity for both cases tends toward a steady state, but the lighter particle ($\rho^* = 0$) maintains a higher velocity. For higher slip lengths, λ_1, both density cases show increased velocity, though the difference in velocity between $\rho^* = 0$ and $\rho^* = 1$ is more pronounced at smaller λ_1 values, where drag effects dominate. As $\rho^* \to \infty$, the particle's motion becomes nearly negligible due to its large inertia. Here, the slip length λ_1 and other hydrodynamic factors have minimal impact, and the particle essentially remains stationary under the applied force.

The plot in Fig. 3(c) shows the normalized velocity of the particle for different particle-to-cavity radius ratios, σ. When $\sigma = 0.1$, this represents a small particle in a relatively large cavity. The particle experiences less influence from the cavity walls, allowing it to move more freely and resulting in higher normalized velocities, particularly for large slip lengths, λ_1. When $\sigma = 0.5$, the particle is larger compared to the $\sigma = 0.1$ case, so the cavity walls have a more noticeable impact on its movement, slightly reducing the normalized velocity. For $\sigma = 1$, the particle and cavity are nearly the same size, placing the particle close to the cavity walls. This proximity significantly increases hydrodynamic resistance, reducing the particle's normalized velocity, especially at lower slip lengths (small λ_1).In summary, the plot illustrates how the normalized transient velocity of the particle varies with slip length and elapsed time, with significant differences arising from the radius ratio, σ. Smaller particles (small σ) move more freely within the cavity, experiencing less drag, while larger particles (large σ) encounter greater wall effects, reducing their mobility. This insight is valuable for understanding the dynamics of colloidal particles in polymer gels and designing controlled drug delivery systems, where particle mobility can be tuned by adjusting slip properties and confinement.

Fig. 4(a, b) illustrates the normalized transient velocity plotted against the particle-to-medium density ratio, ρ^*, for various values of scaled elapsed time, $\nu t/a^2$. The parameters α (the permeability parameter) and σ (the radius ratio) are varied to explore different cases. In Fig. 4(a), the velocity profile for clear fluid reaches a higher steady-state value, as a clear fluid allows the particle to move more freely. As the permeability parameter increases, the porous medium offers greater resistance (higher inverse permeability), resulting in a lower steady-state velocity. This increased permeability resistance dampens the particle's movement. The zoomed inset at the lower left highlights fine details in the normalized velocity for small values of ρ^*, emphasizing that even slight changes in ρ^* have a measurable impact on velocity in this regime, particularly at low α values. Fig. 4(b) shows that for a larger σ (e.g., $\sigma \to 1$), the particle occupies a larger fraction of the cavity, which restricts its mobility and lowers the transient velocity. Similar to Fig. 4(a), there is an increase in transient velocity over time as it approaches steady state. However, for different values of σ, the steady-state values vary, with lower values of σ (indicating a smaller particle relative to the cavity) allowing higher steady-state velocities. These insights could have implications for applications requiring controlled particle mobility, such as drug delivery systems in porous gels, where the particle's density, the medium's permeability, and cavity constraints can be optimized to achieve desired motion profiles.

Fig. 5(a, b, c) illustrates the variation of the normalized transient velocity $6\pi\widetilde{\mu}aU/F_A$ with respect to the dimensionless elapsed time $\nu t/a^2$ for different values of the relevant parameters. The plots show that the normalized transient velocity $6\pi\widetilde{\mu}aU/F_A$ increases continuously from zero to its steady-state value over time. In a porous medium, higher permeability parameter α values result in slower growth and lower steady-state velocities due to increased resistance, whereas higher slip lengths (λ_1 and λ_2) at the particle and cavity surfaces promote faster growth and higher steady-state velocities by reducing frictional resistance. Additionally, particles with a lower density ratio ρ^* experience faster velocity growth and reach higher steady-state values compared to denser particles, which exhibit slower response due to their greater inertia.

The dimensionless acceleration, $(6\pi\rho a^3/F_A)dU/dt$, of a spherical particle undergoing initial migration is plotted against the scaled time, $\nu t/a^2$, in Fig. 6 (a, b, c), for different values of the density ratio ρ^*, permeability parameter α, particle-to-cavity radius ratio σ, and the slip lengths λ_1, and λ_2. This acceleration monotonically decreases as $\nu t/a^2$ increases, starting from a maximum at $\nu t/a^2 = 0$ and approaching zero as $\nu t/a^2 \to \infty$across the entire range of the parameters ρ^*, α, σ, λ_1, and λ_2.

Fig. 6(a) shows multiple curves for different values of the non-dimensional slip length parameters λ_1 and λ_2. For early time behavior, the normalized transient acceleration is high for all curves, showing that the particle initially accelerates quickly in response to the applied force. Higher slip lengths (both λ_1 and λ_2) lead to higher initial accelerations. This is because slip conditions reduce drag, allowing the particle to respond more rapidly to the force. As time progresses, the acceleration decreases for all curves, indicating a transition phase where the particle's velocity approaches its steady state. At large values of $\nu t/a^2$, the normalized transient acceleration approaches zero for all curves, indicating that the particle has reached steady velocity and is no longer accelerating. Particles with higher slip lengths ($\lambda_1 \to \infty$ and $\lambda_2 \to \infty$) reach steady state slightly faster, as they experience less resistance in the medium. For a given cavity slip length λ_2, increasing λ_1 results in a higher initial acceleration and a more gradual decline over time. This reflects reduced drag on the particle itself. For a given particle slip length λ_1, increasing λ_2 generally results in higher initial acceleration values and extends the transient phase, delaying the particle's stabilization at a steady velocity. Therefore, adjusting λ_1 and λ_2 allows fine-tuning of the particle's transient behavior, which could be critical for applications requiring precise timing of particle responses.

Fig. 6 (b) examines the effects of the relative density ratio ρ^* and the particle slip length λ_1 on transient acceleration. For both slip cases ($\lambda_1 = 0$ and $\lambda_2 = 1$), the normalized transient acceleration is high at small values of $\nu t/a^2$, indicating that the particle begins with a sharp initial response to the applied force. For $\rho^* = 0$ (massless particle), the initial acceleration is the highest, as there is no inertia to slow the particle's response. For $\rho^* = 1$ (density of particle equal to medium), the initial acceleration is slightly lower than for $\rho^* = 0$, indicating that inertia from the particle's own mass begins to moderate the response. For $\rho^* \to \infty$ (very dense particle), the initial acceleration is almost zero, suggesting that the particle is largely inert due to its high mass. At large $\nu t/a^2$, the acceleration for all curves approaches zero, indicating that the particle reaches a steady-state velocity where it no longer accelerates.

Fig. 6 (c) focuses on the effects of the radius ratio σ and the permeability parameter α on the transient acceleration of the particle. For both values of α ($\alpha = 0,\ 1$), the curves show high initial accelerations, with smaller values of σ (i.e., smaller particle relative to cavity size) showing the highest initial acceleration. This suggests that particles with smaller sizes relative to the cavity respond more immediately to the applied force. For $\alpha = 0$ (no porous medium), the initial acceleration is slightly higher compared to $\alpha = 1$. This is due to the absence of resistance from the porous structure, allowing faster response. For $\alpha = 1$, the porous medium slows down the initial response, leading to lower acceleration values compared to the clear fluid case. At large $\nu t/a^2$, the acceleration for all curves approaches zero, indicating that the system has reached a steady-state velocity. These insights can be valuable for applications requiring controlled acceleration and motion of particles within confined spaces. Adjusting the radius ratio and permeability could help optimize particle behavior for processes such as filtration, material design, and drug delivery.

We have sketched some of the streamlines in Fig. 7 to achieve a more complete understanding of the transient migration of a hydrophobic colloidal spherical particle inside a hydrophobic, impermeable, concentric cavity with a combination of the relevant parameters. The streamlines are clearly deflected due to the presence of the impermeable cavity.

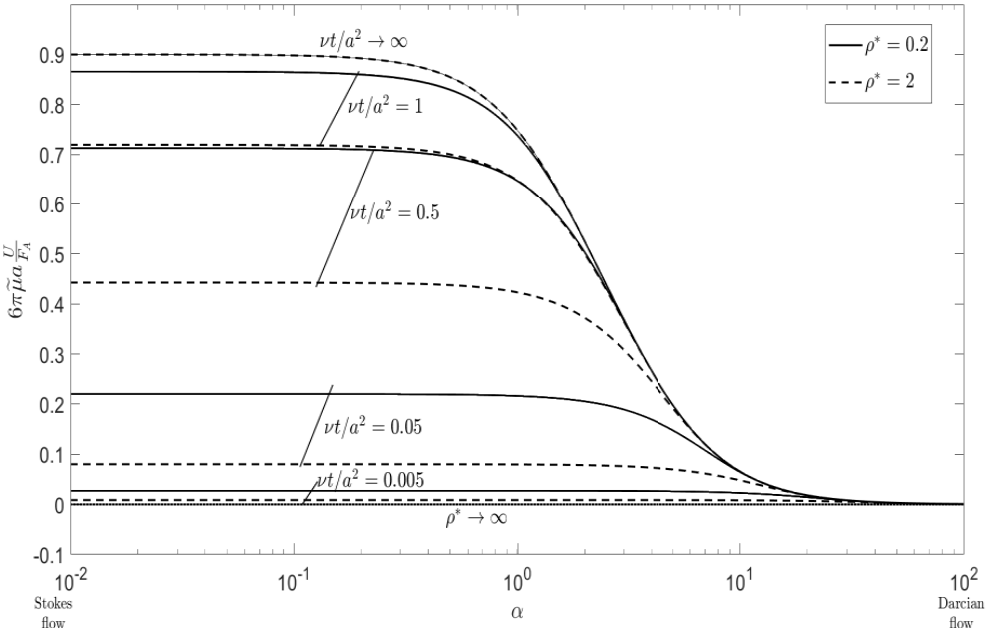

FIGURE 2. Variation of the normalized transient velocity $6\pi\widetilde{\mu}a\frac{U}{F_A}$ versus the permeability parameter α for various values of elapsed time $\nu t/a^2$ in the case of prefect slip surfaces ($\lambda_1, \lambda_2 \to \infty$) and $\sigma = 0.4$.

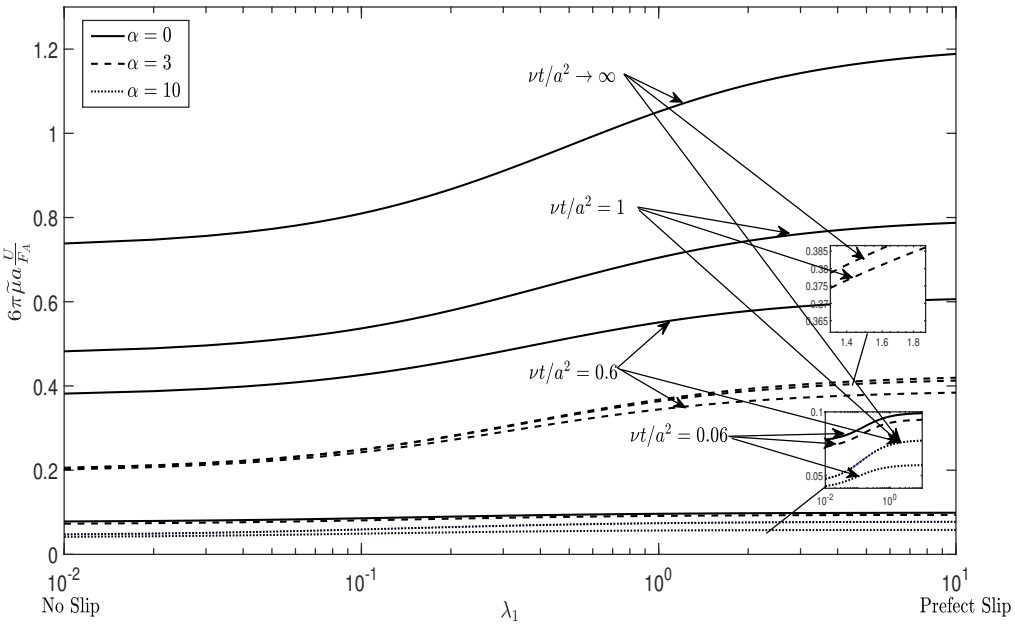
$\alpha = 0$
$\alpha = 3$
$\alpha = 10$
$\nu t/a^2 \to \infty$
$\nu t/a^2 = 1$
$\nu t/a^2 = 0.6$
$\nu t/a^2 = 0.06$
$6\pi\tilde{\mu}a\frac{U}{F_A}$
λ_1
No Slip
Prefect Slip

(a)

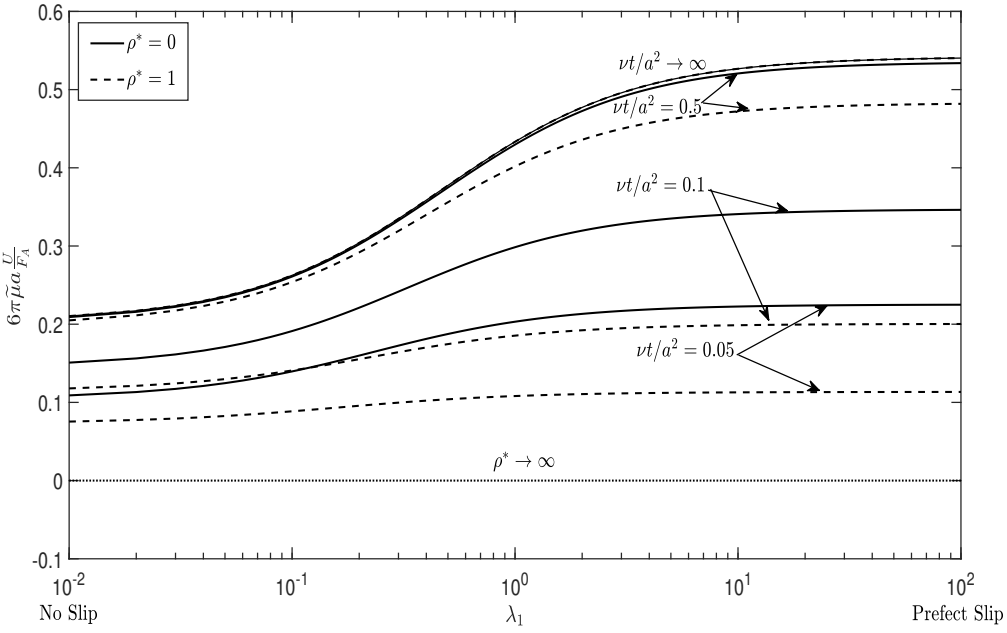
$\rho^* = 0$
$\rho^* = 1$
$\nu t/a^2 \to \infty$
$\nu t/a^2 = 0.5$
$\nu t/a^2 = 0.1$
$\nu t/a^2 = 0.05$
$\rho^* \to \infty$
$6\pi\tilde{\mu}a\frac{U}{F_A}$
λ_1
No Slip
Prefect Slip

(b)

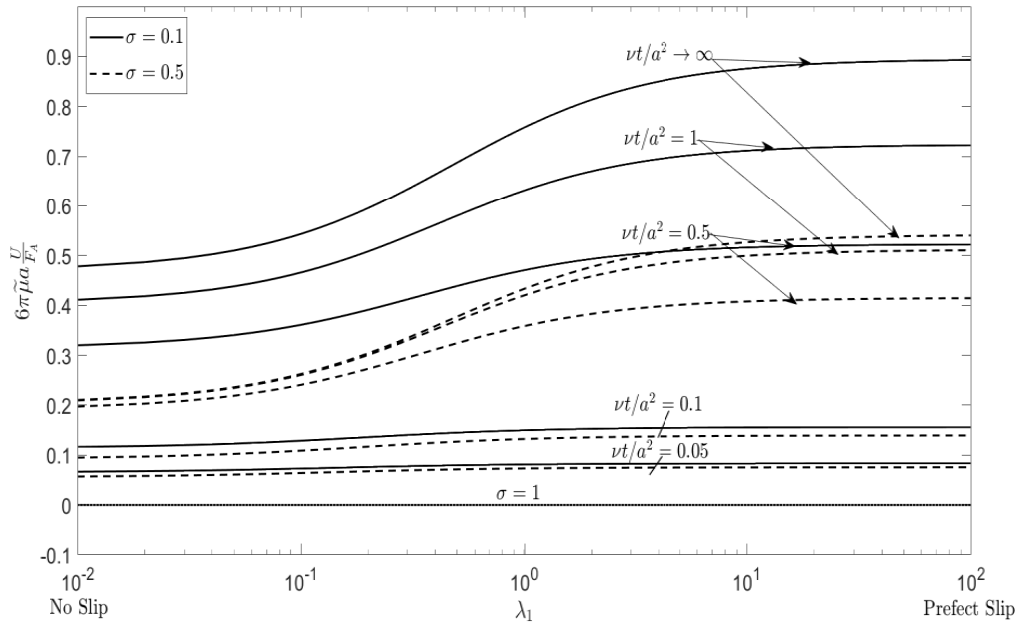

(c)

FIGURE 3. Variation of the normalized transient velocity $6\pi\widetilde{\mu}a\frac{U}{F_A}$ versus the non- dimensional slip length of the particle λ_1 for various values of elapsed time $\nu t/a^2$ in the cases of cavity non-dimensional slip length of the cavity $\lambda_2 = 1$ with versus of permeability parameter α, density ratio ρ^*, and particle-to-cavity radius ratio σ.

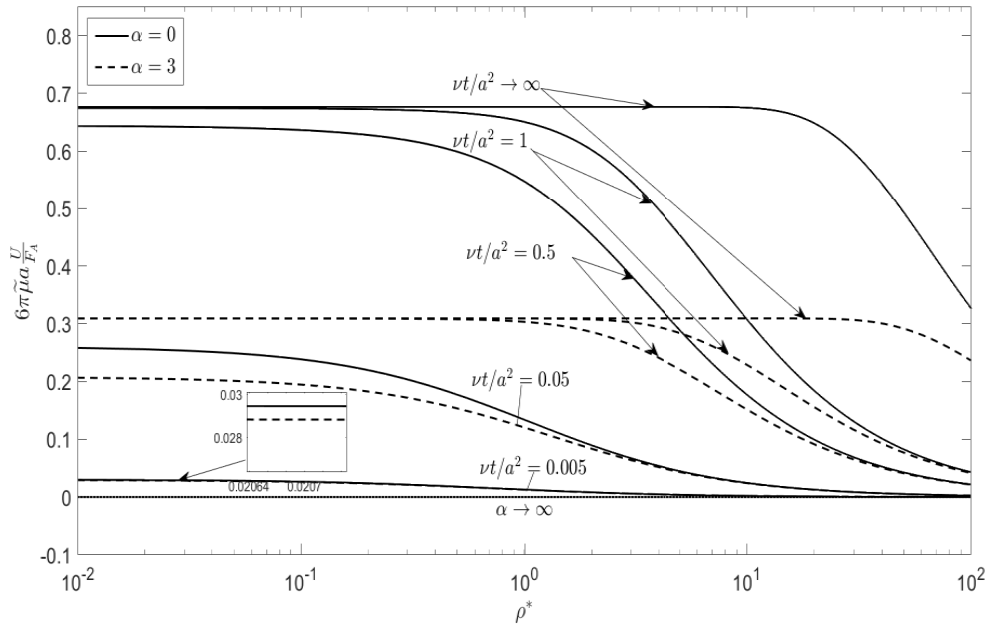

(a)

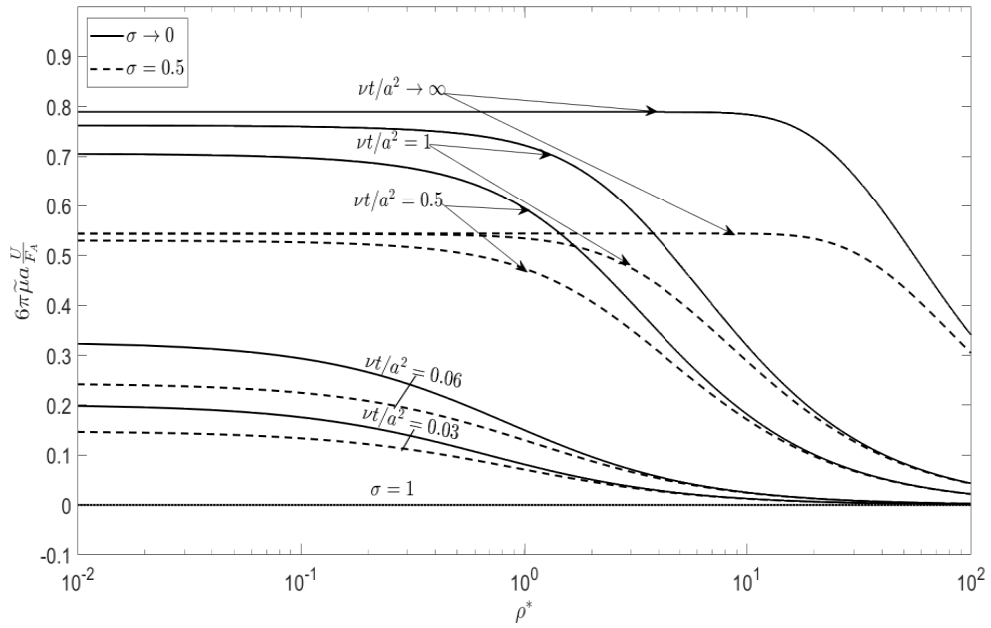

(b)

FIGURE 4. Variation of the normalized transient velocity $6\pi\widetilde{\mu}a\frac{U}{F_A}$ versus particle–to-medium density ratio ρ^* for various values of elapsed time $\nu t/a^2$ in the case of $\lambda_1 = \lambda_2 = 6$ with versus of permeability parameter α, and particle-to-cavity radius ratio σ.

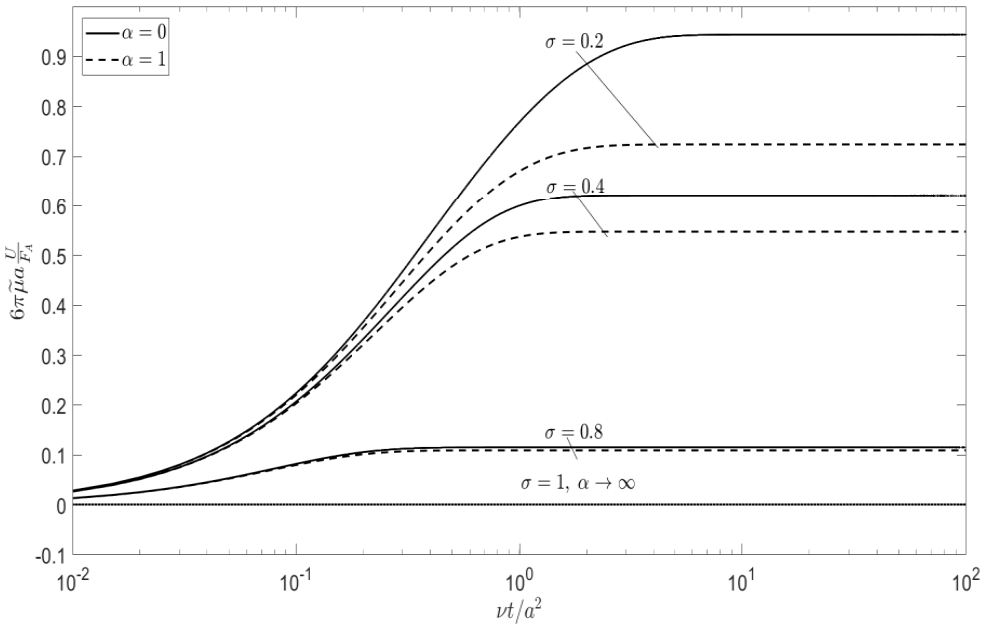
$\alpha = 0$
$\alpha = 1$
$\sigma = 0.2$
$\sigma = 0.4$
$\sigma = 0.8$
$\sigma = 1,\ \alpha \to \infty$
$6\pi\tilde{\mu}a\frac{U}{F_A}$
$\nu t/a^2$

(a)

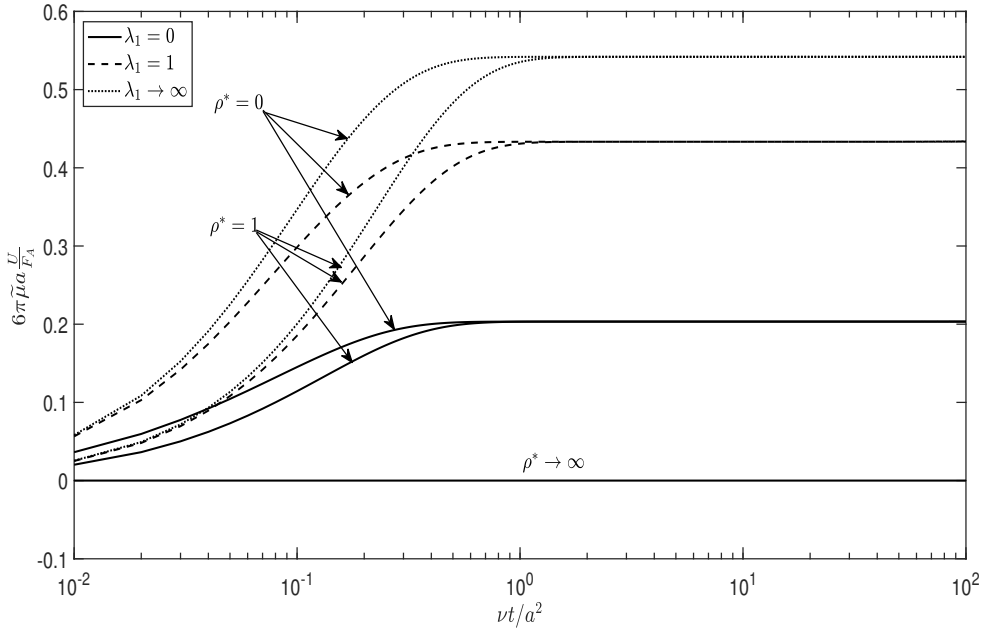
$\lambda_1 = 0$
$\lambda_1 = 1$
$\lambda_1 \to \infty$
$\rho^* = 0$
$\rho^* = 1$
$\rho^* \to \infty$
$6\pi\tilde{\mu}a\frac{U}{F_A}$
$\nu t/a^2$

(b)

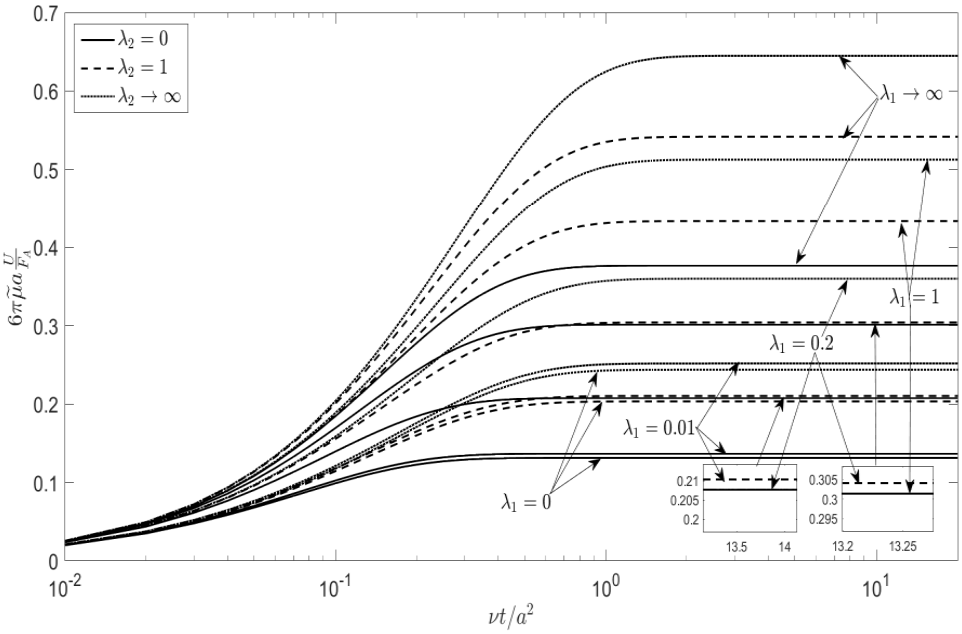

(c)

FIGURE 5. Variation of the normalized transient velocity $6\pi\widetilde{\mu}a\frac{U}{F_A}$ versus the dimensionless elapsed time $\nu t/a^2$ for various values of:
a)particle-to-cavity radius ratio σ and permeability parameter α with $\lambda_1 = \lambda_2 = 1$, $\rho^* = 1$,
b) particle–to-medium density ratio ρ^* in the cases of no slip, partial slip, and prefect slip on the particle surface with $\alpha = 1$, $\sigma = 0.5$, and $\lambda_2 = 1$,
c) non- dimensional slip length of the particle λ_1 in the cases of no slip, partial slip, and prefect slip on the cavity surface with $\alpha = 1$, $\sigma = 0.5$, and $\rho^* = 1$.

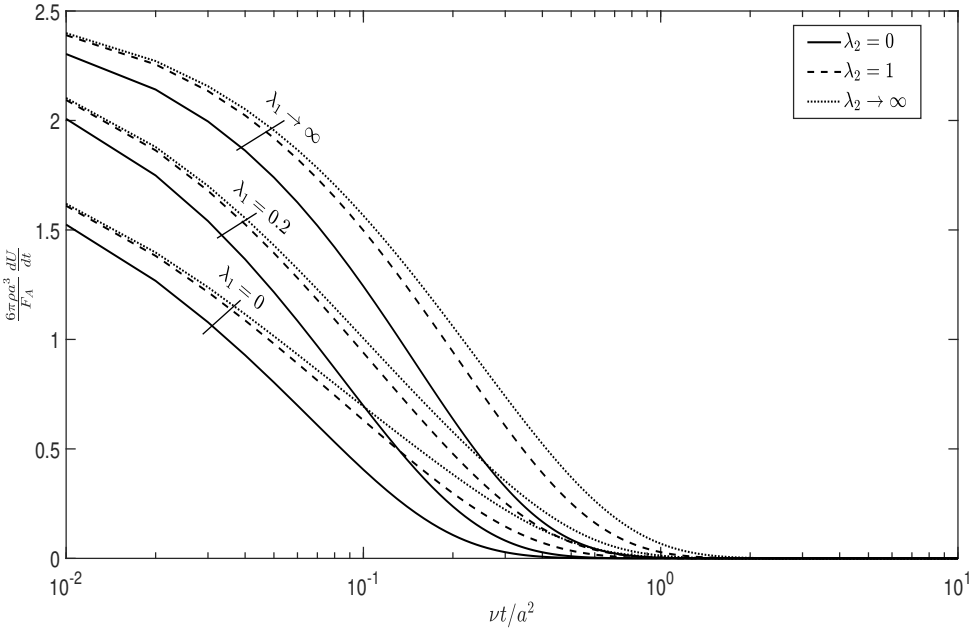
2.5
2
1.5
1
0.5
0
10^{-2}
10^{-1}
10^{0}
10^{1}
$\frac{6\pi\rho a^3}{F_A}\frac{dU}{dt}$
$\nu t/a^2$
$\lambda_2 = 0$
$\lambda_2 = 1$
$\lambda_2 \to \infty$
$\lambda_1 \to \infty$
$\lambda_1 = 0.2$
$\lambda_1 = 0$

(a)

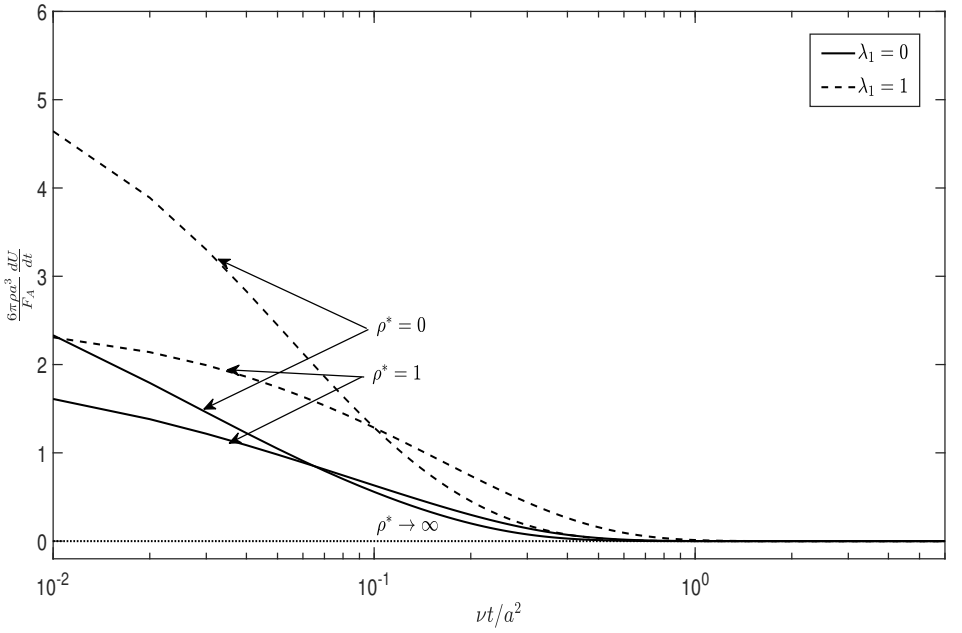
6
5
4
3
2
1
0
10^{-2}
10^{-1}
10^{0}
$\frac{6\pi\rho a^3}{F_A}\frac{dU}{dt}$
$\nu t/a^2$
$\lambda_1 = 0$
$\lambda_1 = 1$
$\rho^* = 0$
$\rho^* = 1$
$\rho^* \to \infty$

(b)

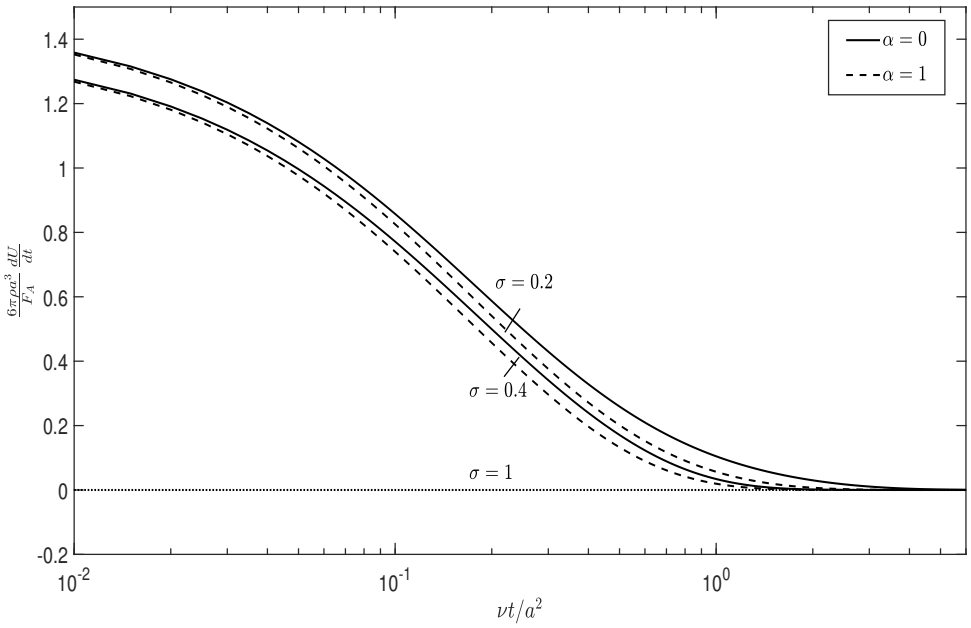

(c)

FIGURE 6. Variation of the normalized acceleration $\frac{6\pi\rho a^3}{F_A}\frac{dU}{dt}$ versus the dimensionless elapsed time $\nu t/a^2$ for various values of:
a) non- dimensional slip length of the particle λ_1 with $\alpha = 1$, $\sigma = 0.5$, and $\rho^* = 1$,
b) particle–to-medium density ratio ρ^* in the cases of no slip, and partial slip on the particle surface with $\alpha = 1$, $\sigma = 0.5$, and $\lambda_2 = 1$,
c) particle-to-cavity radius ratio σ with $\lambda_1 = \lambda_2 = 1$, $\rho^* = 1$, and various values of permeability parameter α.

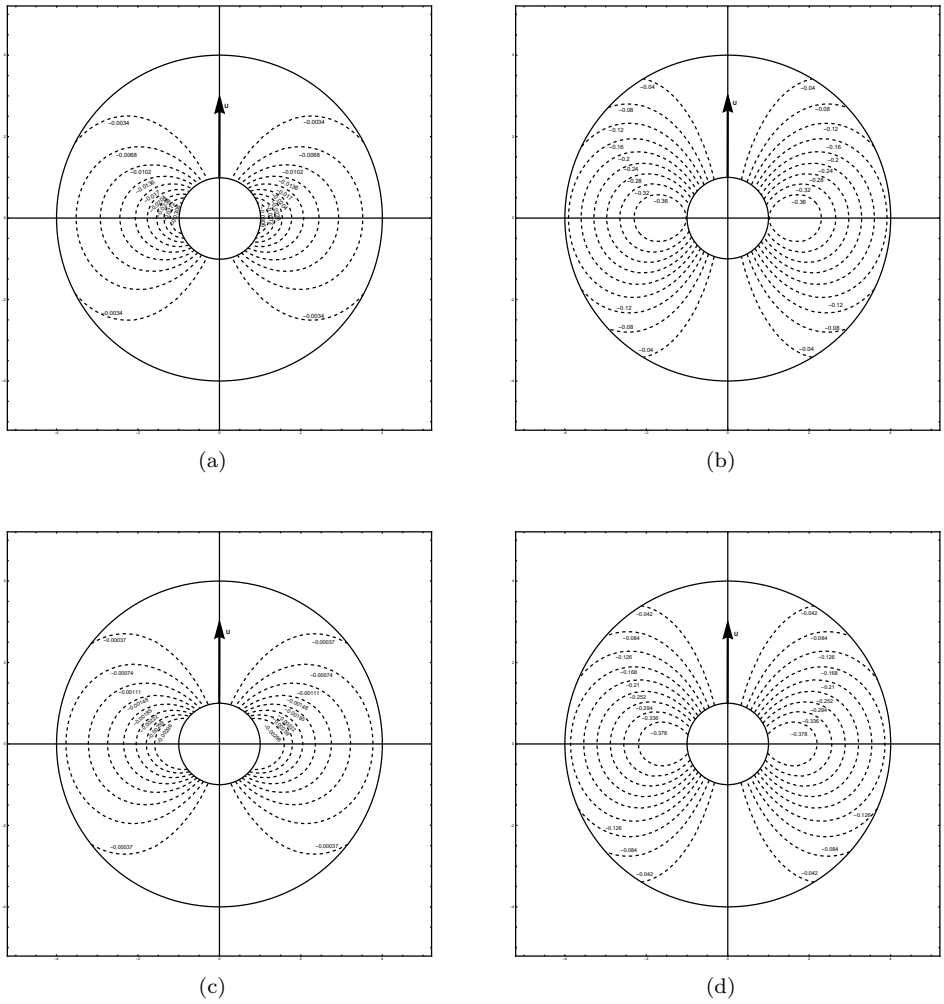

(a) (b)

(c) (d)

FIGURE 7. Sketch of streamlines of the Brinkman transient flow between the particle and cavity:
a) $\alpha = 10,\ \lambda_1 \to \infty,\ \lambda_2 = 0,\ \rho^* = 10,\ \sigma = 0.2,\ \nu t/a^2 = 0.5$,
b) $\alpha = 1,\ \lambda_1 = 1,\ \lambda_2 = 1,\ \rho^* = 1,\ \sigma = 0.2,\ \nu t/a^2 = 1$,
c) $\alpha = 30,\ \lambda_1 = 1,\ \lambda_2 = 1,\ \rho^* = 0.7,\ \sigma = 0.3,\ \nu t/a^2 = 5$,
d) $\alpha = 1,\ \lambda_1 \to \infty,\ \lambda_2 = 1,\ \rho^* = 1,\ \sigma = 0.2,\ \nu t/a^2 = 1$.

5. Conclusions

This work analyzes the transient motion at low Reynolds numbers of a hydrophobic colloidal spherical particle within a concentric cavity with a hydrophobic surface, filled with a polymer gel substance, following the sudden application of a steady body force. The unsteady Brinkman equation governing the fluid velocity

distribution is solved, resulting in a closed form formula for the time-evolving particle velocity in the Laplace transform. Through an examination of the normalized transient velocity and acceleration in low Reynolds number conditions, this analysis provides important insights into the influence of several system parameters, such as the particle to-medium density ratio ρ^*, the scaled elapsed time $\nu t/a^2$, the permeability parameter α, the non-dimensional slip lengths λ_1 and λ_2, and the radius ratio σ. The main findings of this study include the following:

Effect of permeability parameter α

A clear fluid ($\alpha = 0$) allows faster initial responses and higher transient velocities, while the porous medium (higher α) reduces initial acceleration and introduces resistance, slowing down the particle's transition to steady-state velocity. In systems where controlled slowing of particle motion is desired, increasing the permeability parameter can modulate particle movement by adding drag from the porous structure.

Influence of density ratio ρ^*

At higher density ratios, both transient velocity and acceleration decay more quickly, leading to faster stabilization of the particle's motion. Lower density ratios allow the particle to maintain higher velocities over a more extended period. This implies that particles with lower densities relative to the surrounding medium exhibit sustained mobility, which could be advantageous in applications requiring prolonged particle transport.

Effect of slip lengths λ_1 ***and*** λ_2

The slip lengths of the particle and cavity walls influence both transient velocity and acceleration. Higher slip length values (indicating reduced drag at the surfaces) allow the particle to achieve higher initial accelerations and maintain velocity for longer durations. Controlling slip lengths could provide a method to fine-tune particle mobility, which is particularly useful in designing surfaces that require specific frictional characteristics, such as in microfluidic devices or biomedical applications.

Effect of radius ratio σ

Smaller particles relative to the cavity size (σ close to zero) experience higher transient accelerations and take longer to reach steady-state velocities, indicating sustained responsiveness to the applied body force. Larger particles (increasing σ) reach steady-state conditions faster, as confinement effects increase drag. This parameter is crucial when designing systems where particles need to navigate confined environments, as adjusting σ can help regulate the particle's responsiveness and stabilization time.

Time-dependent behavior

The normalized acceleration decreases over time, eventually approaching zero as the particle reaches steady-state velocity. Shorter response times at higher $\nu t/a^2$ values indicate that the system can be optimized for either rapid or prolonged particle motion depending on the application's requirements.

This study provides a comprehensive framework for understanding and controlling the transient motion of particles within porous media, a topic with significant implications for fields such as drug delivery, filtration, and material design. By varying density ratios, permeability, slip lengths, and cavity-to-particle size ratios, it is possible to fine-tune particle behavior to achieve specific dynamic profiles, from rapid stabilization to sustained mobility. It is important to note that the initial transient behavior of a hydrophobic, impermeable particle moving at low Reynolds

numbers within a porous medium enclosed in a hydrophobic cavity has not been previously studied.

6. Conflict of interest

We have no conflict of interest to declare.

7. Data Availability Statement

No data are associated with the manuscript.

References

[1] J. Abate and W. Whitt. A unified framework for numerically inverting Laplace transforms. INFORMS Journal on Computing, 2006, 18: 400-421.
[2] J. Abate and P.P. Valkó. Multi-precision Laplace transform inversion. International Journal for Numerical Methods in Engineering, 2004, 60: 979-993.
[3] S.A. Allison, Y. Xin and H. Pei. Electrophoresis of spheres with uniform zeta potential in a gel modeled as an effective medium. Journal of Colloid and Interface Science, 2007, 313: 328-337.
[4] M. Ayman, E.I. Saad and M.S. Faltas. Transient electrophoresis of a conducting cylindrical colloidal particle suspended in a Brinkman medium. Zeitschrift für Angewandte Mathematik und Physik, 2024, 75: 53.
[5] J.F. Brady. The long-time self-diffusivity in concentrated colloidal dispersions. Journal of Fluid Mechanics, 1994, 272: 109-133.
[6] D.M. Broday. Motion of nanobeads proximate to plasma membranes during single particle tracking. Bulletin of Mathematical Biology, 2002, 64: 531-563.
[7] W.P. Breugem. The effective viscosity of a channel-type porous medium. Physics of Fluids, 2007, 19: 103104.
[8] H.C. Brinkman. A calculation of the viscous force exerted by a flowing fluid on a dense swarm of particles. Applied Scientific Research, 1947, 1: 27-34.
[9] W.Y. Chan and H.J. Keh. Transient slow motion of a porous sphere. Fluid Dynamics Research, 2024, 56: 015503.
[10] E.R. Damiano, D.S. Long, F.H. El-Khatib and T.M. Stace. On the motion of a sphere in a Stokes flow parallel to a Brinkman half-space. Journal of Fluid Mechanics, 2004, 500: 75-101.
[11] R.H. Davis and H.A. Stone. Flow through beds of porous particles. Chemical Engineering Science, 1993, 48: 3993-4005.
[12] P. Debye and A.M. Bueche. Intrinsic viscosity, diffusion, and sedimentation rate of polymers in solution. The Journal of Chemical Physics, 1948, 16: 573-579.
[13] L.H. Dill and R. Balasubramaniam. Unsteady thermocapillary migration of isolated drops in creeping flow. International Journal of Heat and Fluid Flow, 1992, 13: 78-85.
[14] S. El-Sapa. Cell models for micropolar fluid past a porous micropolar fluid sphere with stress jump condition. Physics of Fluids, 2022, 34: 34.
[15] S. El-Sapa. Interaction between a non-concentric rigid sphere immersed in a micropolar fluid and a spherical envelope with slip regime. Journal of Molecular Liquids, 2022, 351: 118611.
[16] S. El-Sapa, E.I. Saad and M.S. Faltas. Axisymmetric motion of two spherical particles in a Brinkman medium with slip surfaces. European Journal of Mechanics - B/Fluids, 2018, 67: 306-313.
[17] M.S. Faltas and S. El-Sapa. Time-periodic electrokinetic analysis of a micropolar fluid flow through hydrophobic microannulus. The European Physical Journal Plus, 2024, 139: 575.
[18] M.S. Faltas, H.H. Sherief, A.A. Allam and B.A. Ahmed. Axisymmetric motion of a slip spherical particle in the presence of a Brinkman interface with stress jump. European Journal of Mechanics - B/Fluids, 2021, 90: 73-88.
[19] M.S. Faltas, H.H. Sherief, A.A. Allam and B.A. Ahmed. Mobilities of a spherical particle straddling the interface of a semi-infinite Brinkman flow. Journal of Fluids Engineering, Transactions of the ASME, 2021, 143: 1-17.

[20] M. Fakour, A. Rahbari, H. Moghadasi, I. Rahimipetroudi, D. Domairry-Ganji and M. Varmazyar. Analytical study of unsteady sedimentation analysis of spherical particle in Newtonian fluid media. Thermal Science, 2018, 22: 847-855.
[21] J. Feng, P. Ganatos and S. Weinbaum. Motion of a sphere near planar confining boundaries in a Brinkman medium. Journal of Fluid Mechanics, 1996, 375: 265-296.
[22] J.R. Gomez-Solanoand and C. Bechinger. Transient dynamics of a colloidal particle driven through a viscoelastic fluid. New Journal of Physics, 2015, 17: 103032.
[23] J.P. Hsu, C.H. Huang and S. Tseng. Gel electrophoresis: importance of concentration-dependent permittivity and double-layer polarization. Chemical Engineering Science, 2012, 84: 574-579.
[24] L. Johansson and J.E. Lofroth. Diffusion and interaction in gels and solutions. 4. Hard sphere Brownian dynamics simulations. The Journal of Chemical Physics, 1993, 98: 7471-7479.
[25] H.J. Keh and Y.C. Huang. Transient electrophoresis of dielectric spheres. Journal of Colloid and Interface Science, 2005, 291: 282-291.
[26] S. Kim and W.B. Russel. The hydrodynamic interactions between two spheres in a Brinkman medium. Journal of Fluid Mechanics, 1985, 154: 253-268.
[27] Y.C. Lai and H.J. Keh. Transient electrophoresis of a charged porous particle. Electrophoresis, 2020, 41: 259-265.
[28] Y.C. Lai and H.J. Keh. Transient electrophoresis in a suspension of charged particles with arbitrary electric double layers. Electrophoresis, 2021, 42: 2126-2133.
[29] M.X. Li and H.J. Keh. Start-up electrophoresis of a cylindrical particle with arbitrary double layer thickness. The Journal of Physical Chemistry B, 2020, 124: 9967-9973.
[30] M.X. Li and H.J. Keh. Transient rotation of a spherical particle in a concentric cavity with slip surfaces. Fluid Dynamics Research, 2021, 53: 045509.
[31] K.P. Madasu, M. Kaur and T. Bucha. Slow motion past a spheroid implanted in a Brinkman medium: Slip condition. International Journal of Applied and Computational Mathematics, 2021, 7: 162.
[32] E.E. Michaelides. Review - The transient equation of motion for particles, bubbles, and droplets. Journal of Fluids Engineering, 1997, 119: 233-247.
[33] A. Mohan, M. Santhamoorthy, T.T.V. Phan and S.C. Kim. Thermoresponsive copolymer hydrogel for hydrophobic and hydrophilic drug delivery. Gels, 2024, 10: 184.
[34] F.A. Morrison and L.D. Reed. Unsteady creeping motion of a sphere at small values of Knudsen number. Journal of Aerosol Science, 1975, 6: 9-18.
[35] M.E. O'Neill and B.S. Bhatt. Slow motion of a solid sphere in the presence of a naturally permeable surface. The Quarterly Journal of Mechanics and Applied Mathematics, 1991, 44: 91-104.
[36] A.R. Premlata and H.-H. Wei. Re-entrant history force transition for stick-slip Janus swimmers: mixed Basset and slip-induced memory effects. Journal of Fluid Mechanics, 2020, 882: A7.
[37] B.C. Roy and E.R. Damiano. On the motion of a porous sphere in a Stokes flow parallel to a planar confining boundary. Journal of Fluid Mechanics, 2008, 606: 75-104.
[38] E.I. Saad. Time-varying Brinkman electrophoresis of a charged cylinder-in-cell model. European Journal of Mechanics - B/Fluids, 2020, 79: 357-366.
[39] E.I. Saad. Start-up Brinkman electrophoresis of a dielectric sphere for Happel and Kuwabara models. Mathematical Methods in the Applied Sciences, 2018, 41: 9578-9591.
[40] E.I. Saad and M.S. Faltas. Time-dependent electrophoresis of a dielectric spherical particle embedded in Brinkman medium. Journal of Applied Mathematics and Physics, 2018, 69: 1-18.
[41] V. Sharanya and G.P. Raja Sekhar. Thermocapillary migration of a spherical drop in an arbitrary transient Stokes flow. Physics of Fluids, 2015, 27: 063104.
[42] H.H. Sherief, M.S. Faltas and K.E. Ragab. Transient electrophoresis of a conducting spherical particle embedded in an electrolyte-saturated Brinkman medium. Electrophoresis, 2021, 42: 1636-1647.
[43] Y.E. Solomentsev and J.L. Anderson. Rotation of a sphere in Brinkman fluids. Physics of Fluids, 1996, 8: 1119-1121.
[44] H. Stehfest. Algorithm 368: Numerical inversion of Laplace transforms. Communications of the ACM, 1970, 13: 47-49.

[45] N.H. Thang, T.B. Chien and D.X. Cuong. Polymer-based hydrogels applied in drug delivery: An overview. Gels, 2023, 9: 523.
[46] P. Tsai, C.H. Huang and E. Lee. Electrophoresis of a charged colloidal particle in porous media: boundary effect of a solid plane. Langmuir, 2011, 27: 13481-13488.
[47] G. Yossifon, I. Frankel and T. Miloh. Macro-scale description of transient electro-kinetic phenomena over polarizable dielectric solids. Journal of Fluid Mechanics, 2009, 620: 241-262.

M.S. Faltas
Department of Mathematics and Computer Science, Faculty of Science, Alexandria University, Alexandria, Egypt
Email address: faltas50@yahoo.com, msfaltas@alexu.edu.eg

E.I. Saad
Department of Mathematics, Faculty of Science, Damanhour University, Damanhour, Egypt
Email address: elssaad@sci.dmu.edu.eg

H.H. Sherief
Department of Mathematics and Computer Science, Faculty of Science, Alexandria University, Alexandria, Egypt
Email address: hhsherief@gmail.com

A.S.Aamer
Department of Mathematics and Computer Science, Faculty of Science, Alexandria University, Alexandria, Egypt
Email address: ahmed.saeed.math@gmail.com, ahmed.saeed_pg@alexu.edu.eg